SANDIA REPORT
SAND2017-10221
Unlimited Release
Printed August 2017

Advanced and Exploratory Shock Sensing Mechanisms

Nicholas H. Nelsen, James D. Kolb, Akshay G. Kulkarni, Zachary Sorscher, Clayton D. Habing, Allen Mathis, & Zachary J. Beller

Prepared by
Sandia National Laboratories
Albuquerque, New Mexico 87185 and Livermore, California 94550

Sandia National Laboratories is a multimission laboratory managed and operated by National Technology and Engineering Solutions of Sandia, LLC, a wholly owned subsidiary of Honeywell International, Inc., for the U.S. Department of Energy's National Nuclear Security Administration under contract DE-NA0003525.

Issued by Sandia National Laboratories, operated for the United States Department of Energy by National Technology and Engineering Solutions of Sandia, LLC.

Available to DOE and DOE contractors from
U.S. Department of Energy
Office of Scientific and Technical Information
P.O. Box 62
Oak Ridge, TN 37831

Telephone: (865) 576-8401
Facsimile: (865) 576-5728
E-Mail: reports@osti.gov
Online ordering: http://www.osti.gov/scitech

Available to the public from
U.S. Department of Commerce
National Technical Information Service
5301 Shawnee Rd
Alexandria, VA 22312

Telephone: (800) 553-6847
Facsimile: (703) 605-6900
E-Mail: orders@ntis.gov
Online order: http://www.ntis.gov/search

SAND2017-10221
Printed August 2017
Unlimited Release

Advanced and Exploratory Shock Sensing Mechanisms

Nicholas H. Nelsen[1], James D. Kolb[1], Akshay G. Kulkarni[2], Zachary Sorscher[2], Clayton D. Habing[3], Allen Mathis[4], Zachary J. Beller[2]

Departments 2276[1], 2241[2], 2279[3], 1556[4]
Sandia National Laboratories
P. O. Box 5800
Albuquerque, New Mexico 87185

Abstract

Mechanical component response to shock environments must be predictable in order to ensure reliability and safety. Whether the shock input results from accidental drops during transportation to projectile impact scenarios, the system must irreversibly transition into a safe state that is incapable of triggering the component. With this critical need in mind, the 2017 Nuclear Weapons Summer Product Realization Institute (NW SPRINT) program objective sought the design of a passive shock failsafe with emphasis on additively manufactured (AM) components. Team Advanced and Exploratory (A&E) responded to the challenge by designing and delivering multiple passive shock sensing mechanisms that activate within a prescribed mechanical shock threshold. These AM failsafe designs were tuned and validated using analytical and computational techniques including the shock response spectrum (SRS) and finite element analysis (FEA). After rapid prototyping, the devices experienced physical shock tests conducted on Sandia drop tables to experimentally verify performance.

Keywords: Additive manufacturing, dynamic system, failsafe, finite element analysis, mechanical shock, NW SPRINT, shock response spectrum

ACKNOWLEDGMENTS

This research was supported by Departments 2276, 2241, 2279, 1556, 2616, 9430 and all of those who made the 2017 NW SPRINT program possible. This includes, but is not limited to, the following: Jared McLaughlin, Colin Smithpeter, and Tommy Woodall, Senior Manager Sponsors; Fran Current, Lindsay Klennert, Nick Leathe, and Audrey Morris-Eckart, Leadership Team; Joseph Martinez, 3D printing; Brian Platzbecker, material and supply acquisition; Eric Langlois and Todd Monson, expert advice and technical discussion. In particular, we would like to thank Clint Holtey (2241), Sita Mani (2241), and Brandon Moore (2241) for their expertise and guidance throughout this competition process each and every week.

Sandia National Laboratories is a multimission laboratory managed and operated by National Technology and Engineering Solutions of Sandia, LLC, a wholly owned subsidiary of Honeywell International, Inc., for the U.S. Department of Energy's National Nuclear Security Administration under contract DE-NA0003525. This work is an independent product of the authors and does not necessarily reflect views held by either Sandia National Laboratories or the U.S. Department of Energy.

TABLE OF CONTENTS

FIGURES

TABLES

1. INTRODUCTION

Mechanical shocks are ubiquitous in a wide variety of industries and research settings. Examples are wide ranging, including transportation of products, explosions, human joints impacts, earthquakes, or accidental drops. All of these events have a common trait: a rapid change of acceleration and release of energy. A mechanical shock is defined as a vector characterizing a transient physical excitation that results in sudden acceleration (Broch 1980). These pulses typically have units of *g*, a multiple of the acceleration due to gravity, and act on very small time scales compared to the system of interest. Due to this transient nature of shock inputs, a static analysis is wholly inadequate to capture the physics of the system. Dynamic events vary with time, across a range of time scales; thus, emphasis must be placed on first principles dynamic system response.

Shock environments have great significance in the nuclear weapons complex, in which safety and reliability are primary concerns. The loads imparted by shocks can impact performance and ultimately cause failure in mechanical and electrical systems. At Sandia National Laboratories, the summer intern design competition Nuclear Weapons Summer Product Realization Institute (NW SPRINT) recognized the importance of designing components to withstand anomalous mechanical shocks, and thus chose this topic as the basis for the summer 2017 challenge.

NW SPRINT is a young program at Sandia National Laboratories that emphasizes rapid development of new and innovative concepts over a compressed summer timeline. The contest runs for eight weeks, in which multiple teams with non-traditional and diverse backgrounds work to utilize new technologies and theories to design, analyze, fabricate, and test a functional device. Emphasis is placed on taking advantage of advances in additive manufacturing (AM), such as multi-material capabilities and topology optimization methods, and on identifying new methods to address obstacles that afflict current technology and equipment. Teams compete to create the best design and will defend their projects in a presentation to technical staff members, managers, and other researchers from both within and outside the Laboratory.

The 2017 NW SPRINT program objective called upon three teams to develop an AM shock failsafe device. This device must be able to trigger in such a way to isolate electrical energy in the system of interest, as a response to input shock energy in abnormal operating environments. This process must be irreversible, in the event of future or periodic shock events. According to the specific objectives sought by the 2017 NW SPRINT program, the shock failsafe device must:

a. Be greater than 75% produced using Additive Manufacturing
b. Fit within an 8 by 8 by 8 inch cubic mechanical envelope
c. Contain at least one electrical channel
d. Have a maximum channel resistance of 10 Ω in its untriggered state
e. Have a minimum channel resistance of 1 MΩ in its triggered state
f. Remain in its untriggered state at or below a 250 *g*, 1 millisecond (ms) haversine shock input

g. Irreversibly and passively trigger at or above a 500 *g*, 1 ms haversine shock input

h. Sense shock input in at least one axial direction

i. Be physically shock tested on a drop table

In addition, stretch goals for well-qualified teams included 100% of device produced using AM, utilization of topology optimization software in component design, inclusion of embedded sensors to evaluate component health, and ability to sense shock input in multiple axial directions. Team A&E made strides in accomplishing the latter two items, as will be described in this report.

Clearly, the essence of the program involves the design of a passive shock failsafe component that breaks an electrical channel contact when exposed to a large threshold acceleration loading from a prescribed input mechanical shock. This work does not consider electric, thermal, or fluid-driven shocks. Further, the device is only required to sense the mechanical shock in one chosen axial direction, but ideas for a more omnidirectional approach will be described herein.

This paper will detail Team Advanced and Exploratory's (A&E) design approach to this challenging problem, the methods used to analyze the merit of those designs, and describe two final failsafe designs. In particular, the shock response spectrum method and finite element analysis provided early design targets that eliminated the need for excess prototyping and provided justifiable decisions for dimensioning and tolerancing components. A combined analytical, computational, and experimental approach serves to validate and verify the shock sensing mechanisms and pave a path for future analysis of modified shock failsafe designs. We close with a discussion of future directions and improvements.

This page is intentionally left blank.

2. SHOCK CHARACTERISTICS

A shock is a physical excitation exhibiting vibratory effects, with a total duration that is commonly less than twice the natural period of the dynamic system of interest (Lalanne 2009). The physical quantity represented by the magnitude of the shock can be force, acceleration, velocity, or displacement, depending on the application. We typically call such a physical shock a *mechanical shock* when the quantity described is acceleration or force. Mechanical shocks transmit kinetic energy to a system.

Ideal shocks have easily representable mathematical expressions, whereas shocks measured from the physical world contain high frequency noise and vibration content that cannot be described with a simple transcendental formula. Some standard shock waveform pulses include the half-sine, square, sawtooth, or haversine (versed sine). All of these types have different associated velocity changes and Fourier spectra, and are encountered in varying physical situations. Given the shock amplitude, duration, and type, we can completely determine all of the information embedded in an ideal shock. The *haversine* is a common waveform that models shock environments due to drops and will be the mechanical shock waveform considered throughout the rest of this report.

2.1. Time Series Analysis

A haversine can qualitatively be described as the segment between two local minimums of a sine wave. Mathematically, the haversine pulse shape with amplitude A and duration T is given by $A\sin^2(\pi t/T)$ and through a trigonometric identify the full waveform is expressed piecewise as:

$$f(t) = \begin{cases} \frac{A}{2}\left(1 - \cos\frac{2\pi t}{T}\right), & t \in [0, T] \\ 0, & \text{else} \end{cases}$$

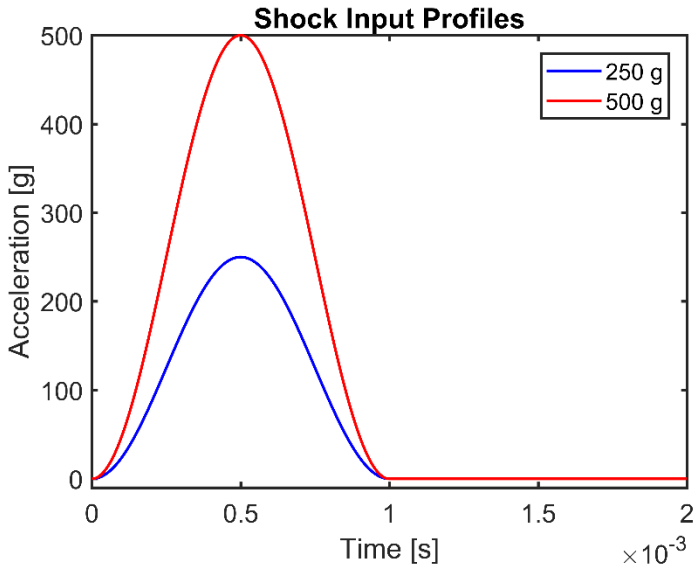

Figure 1. Haversine input shock waveforms

It is important to note that the shock is zero at all values outside the closed interval $[0, T]$, and one cannot simply treat the function as periodic outside this interval. From this simple expression, the kinematics of the shock itself can be derived, by prescribing appropriate boundary conditions (BCs). For velocity, it is sensible to force the function to have some initial velocity (at the impact event, for instance), and then zero velocity at the end of the shock at time $t = T$. Then, the velocity imparted by the acceleration pulse is given by integrating the acceleration waveform and solving for the initial velocity using the appropriate BCs:

$$v(t) = \int \frac{A}{2}\left(1 - \cos\frac{2\pi t}{T}\right) dt = \frac{At}{2} - \frac{AT}{4\pi}\sin\left(\frac{2\pi t}{T}\right) + C$$

$$v(T) = 0 \longrightarrow C = -\frac{AT}{2} = v(0)$$

$$v(t) = \begin{cases} \frac{A}{2}\left[t - \frac{T}{2\pi}\sin\left(\frac{2\pi t}{T}\right)\right] - \frac{AT}{2}, & t \epsilon [0, T] \\ 0\,, & \text{else} \end{cases}$$

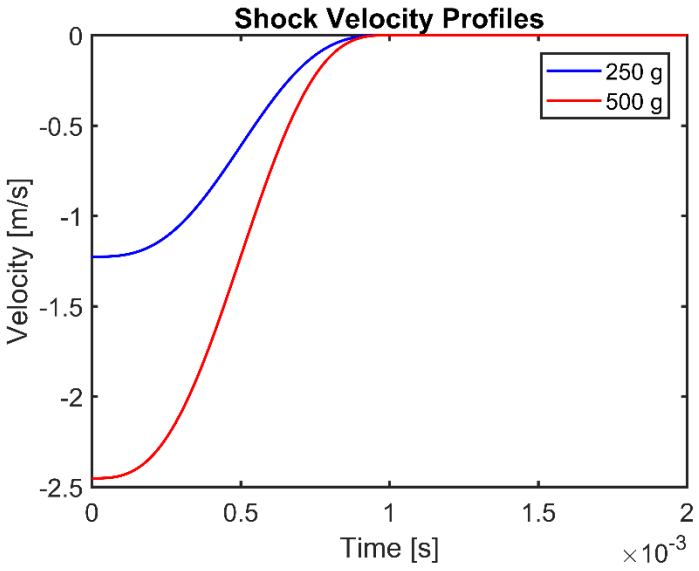

Figure 2. Shock velocities with chosen BCs

We can also interpret the initial velocity $-AT/2$ as the velocity change ΔV, or area under the haversine pulse, of the shock. This is an important parameter to control in drop test experiments, for example.

In a similar fashion, the displacement $y(t)$ up to an additive constant imparted by the shock is obtained by integrating the velocity. We choose the initial displacement to be zero, that is, $y(0) = 0$. This initial condition leads to the displacement profile:

$$y(t) = \begin{cases} \frac{A}{2}\left[\frac{t^2}{2} - Tt + \frac{T^2}{4\pi^2}\cos\left(\frac{2\pi t}{T}\right)\right] - \frac{AT^2}{8\pi^2}, & t \in [0, T] \\ 0\,, & \text{else} \end{cases}$$

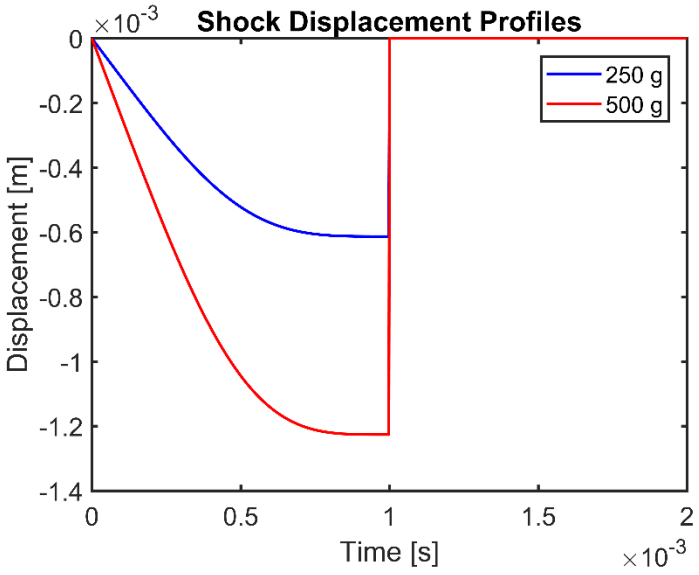

Figure 3. Shock displacements with chosen BCs

These kinematic characterizations of the input haversine shock are of great use when numerically solving the dynamic system that describes the failsafe device of interest, especially when the shock is modeled as an input displacement time series into the base of the system.

To estimate damage potential from the shock, the total energy imparted by the input is computed (Lang 2003). With some test mass *m* chosen from the system, the total mechanical energy *E* due to the shock acceleration $f(t) = \ddot{y}(t)$ with corresponding velocity $v(t) = \dot{y}(t)$ is computed as

$$E = \int_0^T m\ddot{y}(t)\,dx = m\int_0^T \ddot{y}(t)\frac{dy}{dt}dt = m\int_0^T \ddot{y}(t)\dot{y}(t)dt$$

For the haversine input, this mechanical energy computation reduces to

$$E = \frac{mA^2T^2}{8} = \frac{1}{2}m(\Delta V)^2$$

as is expected due to conservation of energy. This approach is significant because it takes into account the entire shock waveform, instead of only picking out the peak loading *A*. In device engineering design, shock energy is a simple method to assign safety factors, prohibit failure, and choose system parameters. Further, the energy of different shock inputs can be compared as a means of identifying and predicting the damage to a mechanical device.

2.2. Fourier Analysis

Shocks are inherently non-periodic phenomena. This transient, pulse-like behavior guarantees that the shock waveform will have its total energy spread across all positive frequencies (Broch 1980), instead of a set of finite frequency values such as in a sinusoidal (thus periodic) series waveform. A careful Fourier analysis will verify this fact; we now derive characteristics for a standard haversine mechanical shock.

The Fourier integral transform is a linear operator that takes a function of some real variable *t* and transforms it into a function of a complex variable ξ. This is termed colloquially as going from the time domain into the "frequency domain", in which the variable ξ in Fourier space is thought of as a "frequency" variable; this interpretation is sufficient for the analysis in this work. Taking the Fourier transform of the input haversine waveform yields, after much work:

$$\begin{aligned}\widehat{f(\xi)} &= \frac{1}{\sqrt{2\pi}}\int_{-\infty}^{\infty} f(t)e^{-i\,\xi t}dt \\ &= \frac{1}{\sqrt{2\pi}}\int_{0}^{T}\frac{A}{2}\left(1-\cos\frac{2\pi t}{T}\right)e^{-i\,\xi t}dt \\ &= \frac{A}{2\sqrt{2\pi}}\left[\frac{ie^{-i\xi T}-i}{\xi}+\frac{\xi ie^{-i\xi T}}{\frac{4\pi^2}{T^2}-\xi^2}-\frac{\xi i}{\frac{4\pi^2}{T^2}-\xi^2}\right]\end{aligned}$$

To extract any relevant frequency information from the Fourier transform, we must now take magnitude of $\widehat{f(\xi)}$ to obtain the *amplitude spectrum* of the haversine shock:

$$\left|\widehat{f(\xi)}\right| = \frac{A}{2\sqrt{\pi}}\left|\frac{1}{\xi}+\frac{\xi}{\frac{4\pi^2}{T^2}-\xi^2}\right|\sqrt{1-\cos(T\xi)}$$

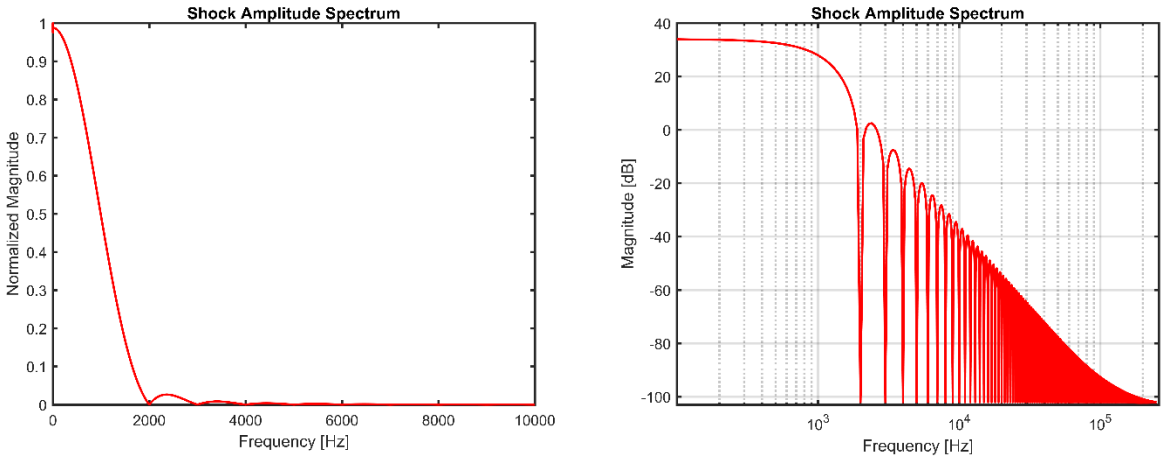

Figure 4. Fourier spectrum of the haversine shock, *A*=500 *& T*=1*ms*

Left: Normalized linear scale, Right: Decibel scale

We observe that indeed the spectrum of the shock is continuous over all nonnegative real frequencies, and no discrete frequency components contribute to resolving the shock. Further, the lobe-like behavior is evident, with zeros at all multiples of $1/T$ starting with the zero $2/T$. In essence, the mechanical shock acts as a low pass filter by emphasizing lower frequencies and damping out the higher frequency content, except at half integer multiples of $1/T$. Although the shock energy is dispersed over all frequencies, its harmonic content indicates that most frequencies above 2000 Hz make inconsequential contributions to the shock amplitude; thus, we would not expect any resonant effects past this threshold and can safely remain within the confines of the period $2T$.

This page is intentionally left blank.

3. DESIGN

3.1. Initial Concepts

Many passive shock sensors are based around the concept of rupturing in some region or breaking some contact under a certain loading threshold. However, due to manufacturing uncertainties and material properties, these types of detectors are quite limited in their scope and reliability (Frangi 2015). Team A&E took a different approach: rather than break, we aim to simply *remove* a contact in an electrical channel, thus forming an open circuit with effectively infinite resistance. Five ideas are presented, in which the last three concepts make full use of this perspective as the design conceptualization stage evolved.

3.1.1. Fuse Devices

Team A&E investigated two worthy fuse mechanisms in terms of shock sensing capabilities, a piezoelectric concept and a solenoid concept. The devices would be required to break a fuse at an acceleration loading of 500 g by generating sufficient current, but not enough current to disable the fuse at 250 g.

Competition regulations state that the resistance of the system must be within 10 ohms. Therefore, the combination of ampere rating and resistance of the fuse resulted in the 80mA and 100mA fuses to be chosen. To break these fuses, a current of 300mA for 0.01 seconds was required based on the current time curve. Our next course of action was to research and test devices that would match the current requirement.

Piezoelectric

Piezoelectric materials respond to vibrations or impacts by generating a pulse of current (Zhang 2011), linking mechanical and electrical energy. For a shock sensor, a fail-safe mechanism would use the current generated by the piezoelectric crystal or film to irreversibly overload a fast-acting fuse and open an electric channel. The magnitude of the impact directly influences the amount of current produced.

Linear electrical behavior governs the piezoelectric material. The linear electric behavior is given by $D = \epsilon E$, where D is the electric displacement, ϵ is the free-body dielectric constant, and E is the electric field strength (Vijaya 2012). Further, piezoelectric materials are elastic, and thus Hooke's law for linear elastic materials is applicable; that is, $E\epsilon = \sigma$ where E is modulus of elasticity, ϵ is strain, and σ is stress. These simple expressions allow for explicit calculation of mechanical and electric properties that could be used to predict piezoelectric behavior upon shock input.

One advantage of a piezoelectric concept is a minimal need for moving parts. These parts would only include wiring, piezoelectric material, film, and a casing. Applications of piezoelectrics are wide ranging and have been proven reliable in many areas. They are utilized frequently in the medical field, in which the piezoelectric material serves as blood pressure, heartbeat, and ultrasonic monitors. However, a major disadvantage of piezoelectric materials is the lack of enough current magnitude (theoretical current calculations in nanocoulombs) to blow a fuse, as

evidenced by preliminary testing. Because of this and other issues, Team A&E did not pursue the piezoelectric concept any further.

Solenoid

The second major fuse mechanism considered was a solenoid shock sensor. Solenoids are common devices that can also convert electrical energy into mechanical energy. A solenoid consists of a magnet placed inside of a helical coil of wire. Based on Faraday's law of induction, the induced electromotive force in any closed circuit is equal to the negative of the time rate of change of the magnetic flux enclosed by the circuit. Therefore, an impact (acting as the electromotive force) would cause the magnet to pass through the coil and induce a current in this coil. We would then design the coil length, magnetic properties, and magnet acceleration to vary the current generated and ultimately overload a fuse.

Team A&E's proposed solenoid design includes a solenoid housing placed in a cylindrical case that allows movement when impacted by a mechanical shock. The wires protruding from the case will connect to the fuse.

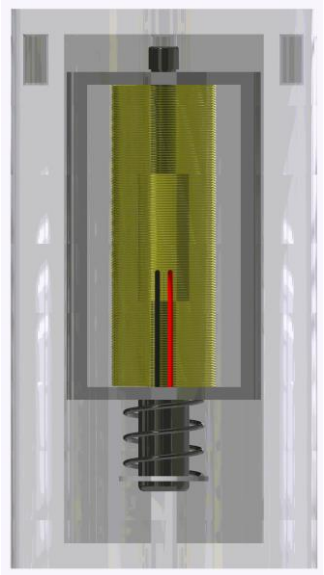

Figure 5. Solenoid initial concept

The solenoid enjoys ease of tuning various component parameters to generate a specific current. It can irreversibly trigger upon correct current input, ensuring minimal malfunction, and the embedded magnets typically have high endurance and resistance to wear. However, a limitation of the solenoid concept is that the current generated from commercially available solenoids is extremely small compared (30mA recorded on multimeter) to predicted current magnitudes required to achieve a 10 ohm electric channel. The device must be fabricated, yet the ability to additively manufacturing solenoid components is outside of the scope of this work. Additionally, problems were expected to arise when designing the circuit to keep the solenoid and electrical leads separate from the fuse circuit.

3.1.2. Spring and Hammer

The spring hammer mechanism is a simple mechanical failure based device. It is a spring mass system where the mass acts as a hammer of sorts. A ceramic wafer will be integrated into the bottom of the system, and the hammer will hit the wafer, opening the circuit, upon a 500 *g* shock.

Figure 6. Spring and Hammer initial concept

Mechanical failure is a predictable situation based on material properties; furthermore, the spring hammer design specifically utilizes brittle fracture as its circuit opening mechanism. Equations governing the fracture of a brittle crystalline material will allow for a ceramic wafer to be designed to shatter upon an impact from the hammer. This ceramic wafer will be an AM part, and it will contain the electrical trace across the fracture zone, effectively opening the circuit upon a brittle fracture.

A linear spring suspending the hammer allows for the impact to be tuned to specific peak acceleration loading using dynamic analysis. In order to fracture the wafer, the hammer must still have energy when it displaces through the ceramic wafer. The fracture strength of the ceramic wafer must be taken into account when designing the displacement and impact velocity of the hammer. Furthermore, a garter spring within the system will allow for the hammer to be as stable and frictionless as possible.

3.1.3. Bistable Beam Mechanism

Bistable beam mechanisms have been utilized in numerous types of electrical and mechanical systems, most notably microelectromechanical systems (MEMS) (Frangi 2015). Their key attribute is bistability; this trait acts as a switch of sorts, in which the elastic beam can buckle into two stable mode shapes. The advantage is that the beam actuation only requires a specific force value to trigger, specifically the contact force exerted by beam inertial mass that passively senses the shock input (Frangi 2015).

Based on previous studies, the beam is prescribed an initial haversine deflection

$$y_0 = \frac{h}{2}\left(1 - \cos\frac{2\pi x}{L}\right)$$

with a corresponding known axial compression load P (Camescasse 2014), and where h is the height of the beam initial deflection and L is the end-to-end line segment length of the beam. After separating space and time variables in the fourth order beam partial differential equation (PDE), a fourth order ordinary differential equation (ODE) in the space variable is obtained. This is a standard Sturm-Liouville eigenvalue problem whose solutions are eigenfunctions (eigenmodes) representing the mode shapes of the bistable beam. Fixed-fixed boundary conditions (BCs) describe the clamped ends, and thus zero Dirichlet and Neumann BCs are assigned for physical reasons. The full solution and analytical expressions for the mode shapes and corresponding eigenfrequencies can be found in Qiu 2004, Cazottes 2009.

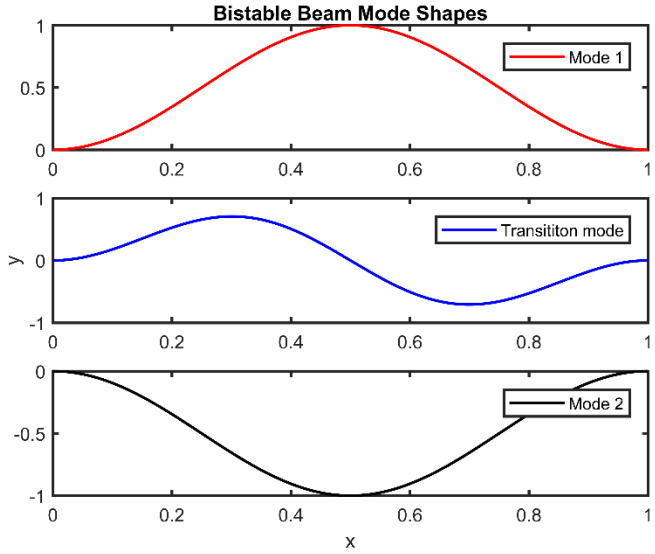

Figure 7. Mode shapes

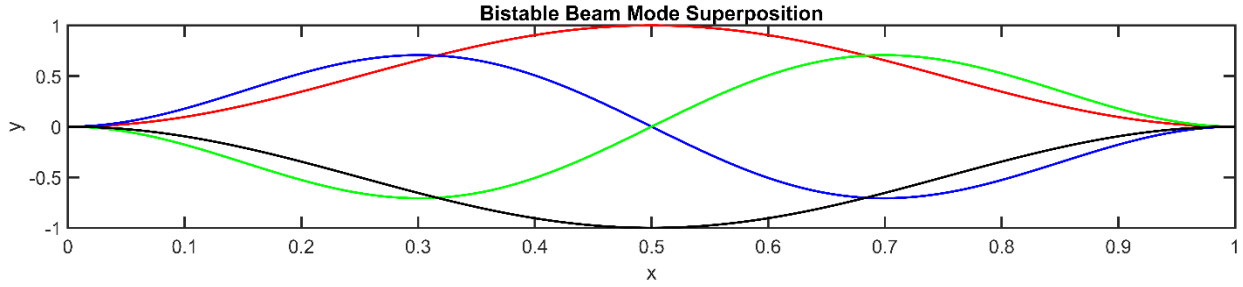

Figure 8. Mode superposition

We follow previous literature (Qiu 2004) by designing a doubly-clamped beam to bolster stability in the second stable buckling mode, which avoids the beam's tendency to twist. Given

the initial deflection y_0 as above, the force required to for the beam to deflect into its second stable mode is

$$F_{mode,12} = \frac{1480EIh}{L^3}$$

and from its second stable mode back in to the first is

$$F_{mode,21} = \frac{1}{2}F_{mode,12}$$

where E is the modulus of elasticity and I is the area moment of inertia (Qiu 2004). These forces are applied as a point load at the midspan of the elastic beam. With these values, we can use dynamic models and the shock response spectrum to design the beam properties to yield these threshold forces upon any shock input. In particular, the design incudes a central rod with spacing for modular weights. This would allow for tuning the natural frequency of the beam in order to achieve the correct acceleration response needed for beam actuation.

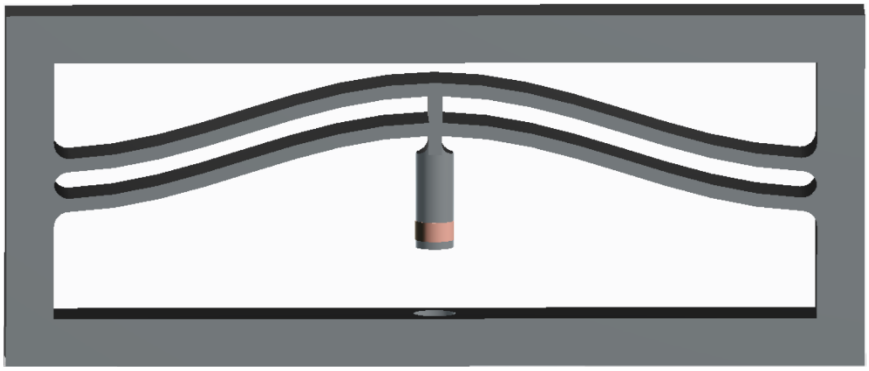

Figure 9. Bistable Beam Mechanism initial concept

Initial prototypes of the bistable beam were 3D printed using a flexible mixture of RGD8560, a preset mixture of the materials Tango and Vero. The beam was prescribed a 0.2 inch width, 2 inch length, 0.2 inch height, and 0.035 inch thickness. Thus, the height-to-thickness ratio $\boldsymbol{Q = h/t}$ value of the prototype was approximately 5.7. This parameter controls the way the beam deflects during actuation, and falls in line with the $\boldsymbol{Q}$ value threshold used by Qiu et al. These dimensions make the area moment of inertia of the beam $\boldsymbol{4 \cdot 10^{-5}}$ in^{-4}. While the test concept demonstrated clear bistable behavior upon force input, it was much too rigid and attempts to correct the flexibility of the material were outside of the resources of available AM capabilities.

3.1.4. Passive Accelerometer Spring System

The goal of the Passive Accelerometer Spring System (PASS) is to create a mechanical accelerometer. An accelerometer is a spring mass damper system that measures the vector acceleration experienced by a body relative to the frame of reference, allowing it to sense vibration, orientation, and shock. Whenever an accelerometer is attached to a falling body, it will detect no acceleration. This occurs because the frame of reference for the accelerometer, the

falling object, is in constant motion with the accelerometer. Upon impact, the accelerometer will sense the vector acceleration the body experiences from the shock.

To create a simple single-axis, single-direction mechanical accelerometer, a mass is fixed to a spring and allowed to travel along the axis of the spring. The acceleration the mass experiences is indicated by the displacement of the mass. The concept with PASS is to open an electric channel once the mass displaces a distance corresponding to a 500 *g* peak acceleration loading. A sprung latching mechanism will actuate at a set displacement corresponding to the 500 *g* shock, the circuit will be removed, and the latch will enter an I-beam shaped channel allowing the mass to continue moving freely without connecting the circuit.

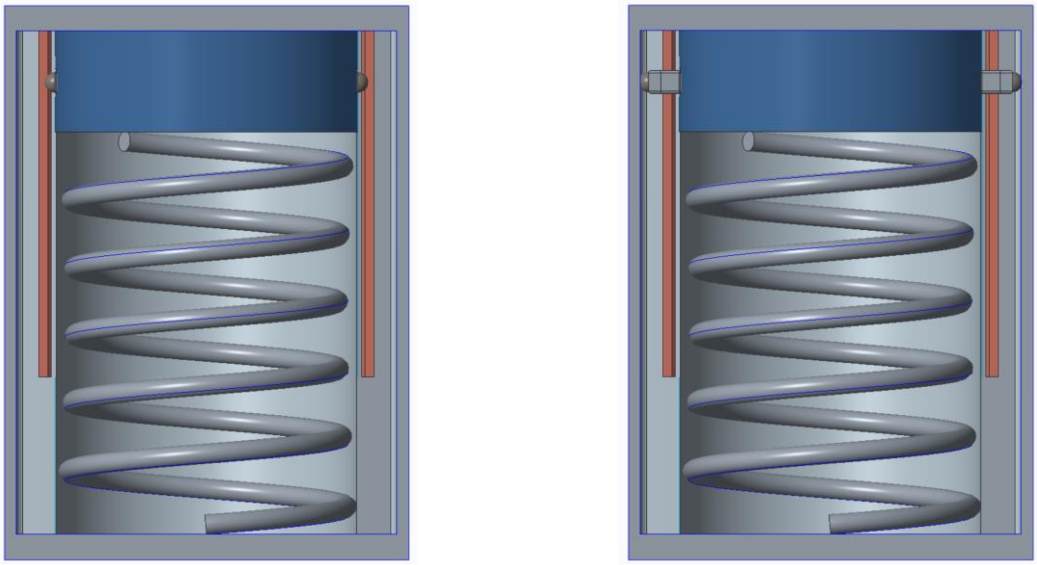

Figure 10. PASS initial concept

Left: Untriggered state, Right: Triggered state

Concerns with the system arise in the latching mechanism and the rigidity of a AM body. Due the spring-loaded latch design, friction may have a considerable effect on the analysis of the system. Furthermore, dynamic analysis of a spring system assumes a rigid body. It is possible that an AM body will not be rigid enough to support the analysis.

3.1.5. Magnetic Shock Failsafe

The objective of the Magnetic Shock Failsafe (MSF) is to detect and trigger at a 500 *g* shock and remain untriggered at 250 *g*. The initial MSF concept consists of a ball bearing, magnet, and an additively manufactured case. On either side of the ball bearing, a 3D printed conductive trace is placed to close the circuit. The attractive force between the magnet and the ball bearing will cause the ball to stay in contact with both ends of the conductive trace. Therefore, in an untriggered position, the ball will stay in place resulting in a completed circuit. With sufficient force, the ball bearing will overcome the magnetic forces and be ejected from the mechanism causing the circuit to break. An exit valve or flap is placed at the end of the channel to ensure that the likelihood of the ball reentering the orifice and closing the electric channel is minimal. This choice satisfies the irreversible actuation requirement.

Figure 11. MSF initial concept

This MSF is designed to mount to an external housing fixture. An advantage of this mechanism is that it can be tuned to various force specifications. To elaborate, different high or low pull (strength) magnets can be placed in the top section to vary the magnet field that the ball bearing will experience. This allows for significant operational flexibility. Additionally, this mechanism has been designed with scalability in mind, such that the structure can be changed significantly to comply with space requirements.

Some challenges include determination of the force between magnets as well as the energy required for the actuating magnet to overcome the pull of the top magnet and exit the valve. The flexibility of 3D printed flaps made of NinjaFlex or SemiFlex proved to be a hindrance because the exiting magnet became stuck in the flap. Finally, omnidirectional operability must be considered since at this state the device can only operate in a single axial direction. Future prototypes will be designed and analyzed to address these concerns.

3.2. Down Selection Process

With a very limited project time, Team A&E decided it was wise to eliminate many choices that posed a large design risk. A pugh matrix attempted to quantify the design risk. Design risk is a loose term, so the criteria for the pugh matrix had to be well thought out and agreed upon. The criteria struck a balance between competition rules, analytical capability, and uniqueness. Pugh matrices were then individually completed and the results were normalized to provide the same weight to each team member's opinions. To further improve the down selection process, a design review with Subject Matter Experts (SMEs) was initiated. All designs were presented, and the results of the pugh matrix were discussed.

The pugh matrix and design review highlighted many concerns with current designs, namely poorly defined material properties for AM materials within the bistable and spring hammer mechanisms, friction within the PASS latching mechanism, and insufficient current generation within the solenoid design. After a few iterations of material selection with the bistable

mechanism, the team believed much of the problems with quantifying material properties could not be overcome with the time constraints of the project. This ultimately led to the abandonment of the bistable mechanism. The spring hammer and solenoid mechanisms were also abandoned due to concerns with creating a reliable breaking mechanism and inability to generate sufficient current, respectively.

The remaining designs, the PASS and the MSF, underwent a second iteration to fix concerns highlighted in the pugh matrix and design review. The PASS was redesigned with ball bearings as the mechanism to open the circuit in order to eliminate friction experienced by the traveling mass, and the MSF was redesigned implementing two bar magnets to allow for a more predictable magnetic calculation. In both, focus was directed to removing contact at the electric channel. After improving these concepts, Team A&E settled for the further investigation of the PASS and MSF designs.

This page is intentionally left blank.

4. MATERIALS AND METHODS

4.1. Shock Response Spectrum

One of the limitations of the spectral description of the haversine shock input from the Fourier analysis in section two is that the amplitude spectrum does not give any indication about the severity of the shock imparted to the relevant mechanical system. This is understandable because the amplitude spectrum is a fundamental characterization of the shock itself and neglects any of the dynamic properties of the system that is actually receiving the shock input. To characterize and predict system response to mechanical shock input, the *shock response spectrum* (SRS) is required (not to be confused with the Fourier amplitude spectrum). Heavily advanced by Dr. David Smallwood at Sandia National Laboratories (Smallwood 1981), the SRS technique allows engineers and scientists to design components to withstand arbitrary shock loading levels and compare the relative severity of two different shocks on a system or device of interest.

The SRS solves for the peak response of an infinite number of single degree of freedom (SDOF) mechanical systems, each with constant damping ratio ζ and continuously increasing natural frequency ω_n. An brief overview of dynamic system theory is presented before delving into the behavior and application of the SRS.

A dynamic system can be mechanical, electrical, thermal, fluid, or any coupled combination of the former. Each system has a set of inherent dynamic properties, termed the damping ratio and the natural frequency, that can be derived from specific elements in the system. These elements in the system can be static or dynamic and active or passive in terms of energy dissipation (Palm 2013). For the simple SDOF second-order mechanical systems in this work, the natural frequency and damping ratio are derived from three components: a lumped parameter mass *m*, a viscous damper with damping coefficient *c*, and a linear elastic spring with constant *k*. This system is often termed a damped harmonic oscillator, with natural frequency given by

$$\omega_n = \sqrt{\frac{k}{m}}\ \frac{rad}{s} = \frac{1}{2\pi}\sqrt{\frac{k}{m}}\ Hz$$

and damping ratio as

$$\zeta = \frac{c}{2m\omega_n} = \frac{c}{2\sqrt{mk}}$$

The damping constant c is typically found using specific experimental methods, while m and k are more easily measured. However, the actual value of c is not necessary if the damping ratio itself is already specified.

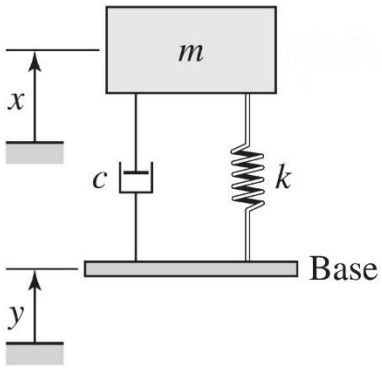

Figure 12. SDOF damped mechanical oscillator

The SDOF damped oscillator represents the physical model of the PASS or bistable mechanism. In the case of the bistable beam, its effective spring constant is a stiffness given by the beam geometry and material properties, and damping would be assumed to be an inherent property of the structure. In this situation, the force that would induce bistable beam actuation would be proportional to the response acceleration of the mass.

Given this model and using Newton's second law, the equation of motion for the mass is

$$\boldsymbol{m\ddot{x} = -c(\dot{x} - \dot{y}) - k(x - y)}$$

or by dividing through by *m* and substituting in the dynamic parameters, we obtain

$$\boldsymbol{\ddot{x} + 2\zeta\omega_n\dot{x} + {\omega_n}^2 x = 2\zeta\omega_n\dot{y} + {\omega_n}^2 y}$$

This governing ordinary differential equation (ODE) is second-order and linear. The transfer function $\boldsymbol{T(s)}$ of this system is obtained by taking the ratio of the Laplace transforms of the output over the input, where initial conditions are assumed to be zero. The response (solution) of any linear dynamic system is given by the convolution of the system's transfer function (or *impulse response function*) with the input excitation. Note that while we use the Laplace transform in this work, the time history response of the system could also be computed as the convolution of the Fourier transforms of both the shock (see section two) and the *frequency response function* (Broch 1980).

Observe that the transfer function of the above ODE can either relate absolute displacement or acceleration because

$$\boldsymbol{\frac{\mathcal{L}\{\ddot{x}\}}{\mathcal{L}\{\ddot{y}\}} = \frac{s^2X(s)}{s^2Y(s)} = \frac{X(s)}{Y(s)} = T(s)}$$

However, its typical use is for acceleration input and output (Smallwood 1981, 1986). We obtain

$$\boldsymbol{T_A(s) = \frac{cs + k}{ms^2 + cs + k} = \frac{2\zeta\omega_n s + \omega_n^2}{s^2 + 2\zeta\omega_n s + \omega_n^2}}$$

This $\boldsymbol{T_A(s)}$ model will be used for all acceleration-based SRS, which applies directly to the functionality and design of the bistable beam mechanism. We used an open source SRS

algorithm (Irvine 2002) in MATLAB for all acceleration response spectrums, and the $\boldsymbol{T_A(s)}$ model verified that this algorithm was producing correct peak acceleration responses.

For systems in which relative displacement is of main concern, a variation of the acceleration-driven equation of motion is derived. Substituting $\boldsymbol{z = x - y}$ as the relative displacement between the mass and the base structure (Smallwood 1986) into the equation of motion for the SDOF oscillator, we obtain

$$\boldsymbol{m\ddot{z} + c\dot{z} + kz = -m\ddot{y}}, \text{ or } \boldsymbol{\ddot{z} + 2\zeta\omega_n\dot{z} + \omega_n^2 z = -\ddot{y}}$$

The transfer function for this relative displacement model is then

$$\boldsymbol{T_D(s) = \frac{-s^2}{s^2 + 2\zeta\omega_n s + \omega_n^2}}$$

Now for any input, the equation of motion can be solved for the absolute acceleration with $\boldsymbol{T_A(s)}$ or the relative displacement response of the mass with $\boldsymbol{T_D(s)}$. This can be done analytically using a convolution integral or numerically in MATLAB. The analytical solution (Gaberson 2007) to the relative displacement model with a haversine shock input $\boldsymbol{\ddot{y}(t)}$ and initial conditions $\boldsymbol{z_0}$ and $\boldsymbol{\dot{z}_0}$ is

$$\begin{aligned}
\boldsymbol{z(t)} &= \boldsymbol{\int_0^t [\mathcal{L}^{-1}\{T_D(s)\}(t-\tau)]\ddot{y}(\tau)\, d\tau} \\
&= \boldsymbol{z_0 e^{-\zeta\omega_n t}\left(\cos\left(t\omega_n\sqrt{1-\zeta^2}\right) + \frac{\zeta}{\sqrt{1-\zeta^2}}\sin\left(t\omega_n\sqrt{1-\zeta^2}\right)\right)} \\
&\quad \boldsymbol{+ \frac{\dot{z}_0 e^{-\zeta\omega_n t}}{\omega_n\sqrt{1-\zeta^2}}\sin\left(t\omega_n\sqrt{1-\zeta^2}\right)} \\
&\quad \boldsymbol{- \frac{1}{\omega_n\sqrt{1-\zeta^2}}\int_0^t \ddot{y}(\tau)\, e^{-\zeta\omega_n(t-\tau)}\sin\left((t-\tau)\omega_n\sqrt{1-\zeta^2}\right)\, d\tau}
\end{aligned}$$

For most shock scenarios in the absence of relative initial displacement and velocity, the above solution reduces down to the last term, which is easily evaluated using digital recursive filters (Smallwood 1981).

Numerical solution involved writing the second-order ODE equation of motion in standard affine dynamical system format

$$\boldsymbol{\frac{d}{dt}Z(t) = A \cdot Z(t) + B}$$

where $\boldsymbol{Z(t)} = \begin{pmatrix} z_1 \\ z_2 \end{pmatrix} = \begin{pmatrix} z(t) \\ \dot{z}(t) \end{pmatrix}$ is a vector of state space variables, $\boldsymbol{A}$ is a constant matrix, and $\boldsymbol{B}$ is a vector of constants. Simplifying, we obtain the coupled first-order matrix system

$$\begin{pmatrix} \dot{z}_1(t) \\ \dot{z}_2(t) \end{pmatrix} = \begin{pmatrix} 0 & 1 \\ -\omega_n^2 & -2\zeta\omega_n \end{pmatrix}\begin{pmatrix} z_1 \\ z_2 \end{pmatrix} + \begin{pmatrix} 0 \\ -\ddot{y} \end{pmatrix} = \begin{pmatrix} z_2 \\ -\omega_n^2 z_1 - 2\zeta\omega_n z_2 - \ddot{y} \end{pmatrix}$$

The solution is then obtained with the MATLAB *ode45* explicit solver. This method is directly applicable to solving the equation of motion for the PASS.

Now we describe the SRS and its applications in design choice and damage prediction. The SRS technique models a complex system as a continuous series of SDOF second-order damped oscillators, each with constant damping ratio $\boldsymbol{\zeta}$ and increasing natural frequency $\boldsymbol{\omega_n}$. The SRS is the peak response of these SDOF systems to the shock input, as a function of the natural frequency of the system. Since many important systems in reality have multiple components, the SRS predicts the peak response of these components to the same mechanical shock input; it does not characterize the mechanical shock itself. This wider, more global approach using the SRS is frequently utilized in the aerospace, oceanic, and seismic industries (Smallwood 1986).

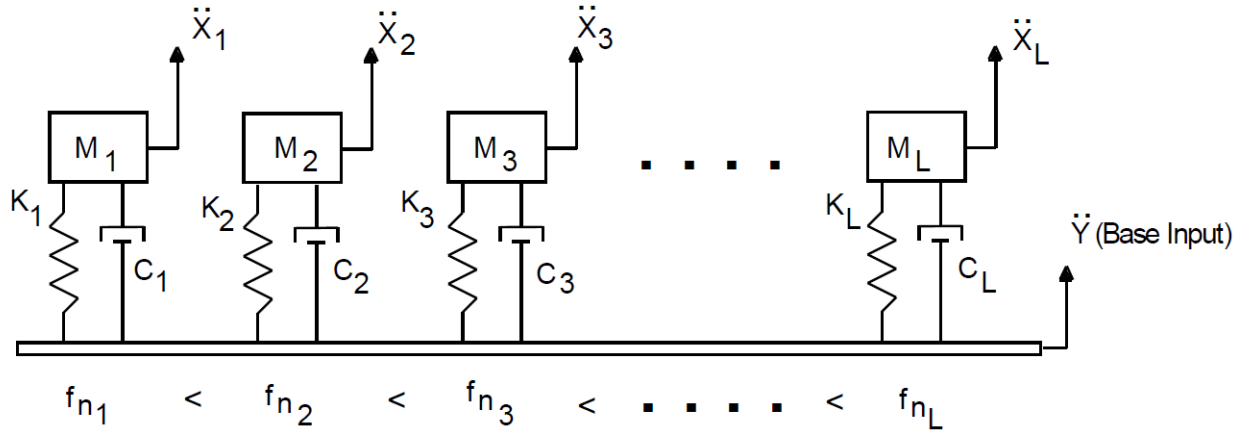

Figure 13. SRS system model (Irvine 2002)

For most applications, the damping ratio is commonly set to 0.05 (5%) (Irvine 2002, Lalanne 2009). As each oscillator becomes stiffer and stiffer as the natural frequency increases, the peak (acceleration) response converges to the peak input shock acceleration (Walter 2005). This is the trend at high frequencies. At low frequencies, the SRS has a constant slope on a logarithmic scale equal to the velocity change of the shock (Smallwood 1994). Scaling of the input shock amplitude behaves linearly on the SRS, while increased shock duration induces a greater slope in the low frequency regime (Lalanne 2009). As seen in the plot of the SRS, there exists some frequency that produces a peak response of the component. If this loading is undesirable, a design engineer could choose to reduce the natural frequency of the component by mounting the part to its base with certain materials or isolators that would effectively lower the spring constant (Irvine 2002). Thus, the damage to the component due to the shock is diminished.

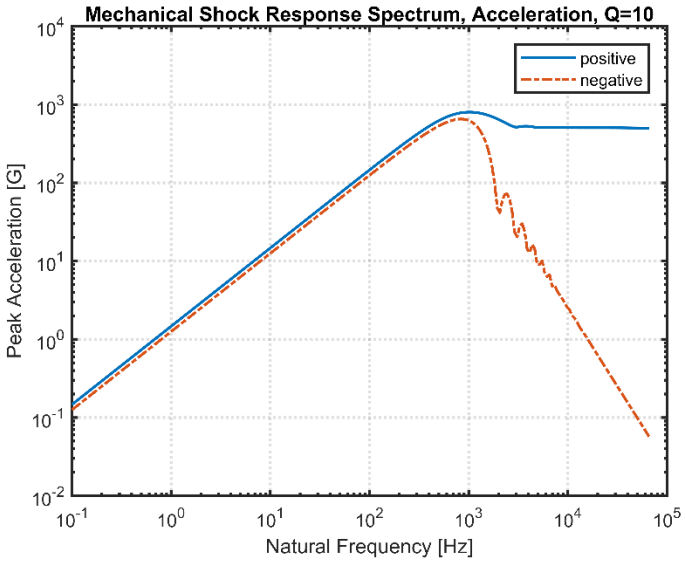

Figure 14. Acceleration SRS, 500 g haversine shock

Additionally, there are many variations of SRS types. For any SRS, the positive and negative peak response curves can be plotted. Other types include the maximax SRS (global maximum response), initial SRS (peak response during the shock duration), and the residual SRS (peak response after the shock excitation) (Broch 1980). In this work, we utilize the maximax SRS to tune the PASS to obtain a desired displacement at the required shock intensity.

4.2. Finite Element and Modal Analysis

The PASS, modeled as a SDOF oscillator, truly is represented by such a system. This inherent simplicity allowed Team A&E to rely on purely a dynamic analysis in solving equations of motion to obtain the response of the PASS. The effect of the structure on this response was assumed to be negligible, due to an assumed damping ratio of 0.05 and rigidity of the AM material. These assumptions are later proved to be acceptable during shock testing.

On the other hand, the MSF cannot be mathematically modeled as a simple mechanical system. The casing structure is composed of irregular geometries that require a more computational analysis. In particular, we seek the eigenmodes and corresponding natural frequencies of the device, as well as fracture analysis in susceptible regions of the design.

The commercial software Abaqus solved both questions. Part material was set to PLA for the AM structure, with Young's Modulus of 3.5 GPa, Poisson's ratio of 0.36, and density of 1240 kg/m^3. The permanent cylindrical magnets inside MSF were given material properties of neodymium, with Young's Modulus of 160 GPa, Poisson's ratio of 0.24, and density of 7500 kg/m^3. Clearly, the PLA is soft compared to neodymium. The 500 g mechanical shock was input into the base of the part in a two-dimensional axisymmetric simulation. After this setup process, fracture and modal simulations were performed.

4.3. Analytical Magnetic Force Model

The MSF relies on the force between two cylindrical permanent magnets to trigger the device upon input shock energy. While many asymptotic formulas using power laws for magnetic attraction forces are widely available, our need for extremely small separation distance between magnet faces required a more accurate expression.

The *exact* magnetostatic attraction force F_z in the axial z-direction due to the interaction of two permanent cylindrical magnets of identical radius is given in a previous study (Vokoun 2009) as

$$F_z = 2\pi\left(\frac{\mu_0 M^2}{2}\right)R^2 \sum_{i=-1}^{1}\sum_{j=-1}^{1} i \cdot j \cdot A_{11}^0(\zeta + i\tau_1 + j\tau_2, 1, 1)$$

where

$$A_{11}^0(\phi, 1, 1) = \frac{\phi}{\pi k_1}E(k_1^2) - \frac{k_1\phi\left(2 + \frac{\phi^2}{2}\right)}{2\pi}K(k_1^2) + \frac{1}{2},$$

$$k_1^2 = \frac{4}{4 + \phi^2},$$

$\mu_0 = 4\pi \cdot 10^{-7}\ N/A^2$ is the permeability of free space, M is the saturation magnetization, R is the magnet radius, $\zeta = Z/R$ is the dimensionless center-to-center distance between the two magnets with center-to-center distance Z, $\tau_i = t_i/2R$, $i\ \epsilon\ \{1, 2\}$, are the dimensionless aspect ratios of the two magnets with thicknesses t_i, and $K(m)$ and $E(m)$ denote the complete elliptic integrals of the first and second kinds, respectively, and are given by

$$K(m) = \int_0^{\frac{\pi}{2}} (1 - m\sin^2\theta)^{-\frac{1}{2}}\, d\theta$$

$$E(m) = \int_0^{\frac{\pi}{2}} (1 - m\sin^2\theta)^{\frac{1}{2}}\, d\theta$$

where *m* is a real number such that $0 < m < 1$ (Good 2001).

This formula assumes the two magnets are equal in cylindrical radius, uniformly magnetized along the axis of symmetry of the cylinders, axially coincident (common axis), curl free, and made of the same material corresponding to saturation magnetization M (Vokoun 2009).

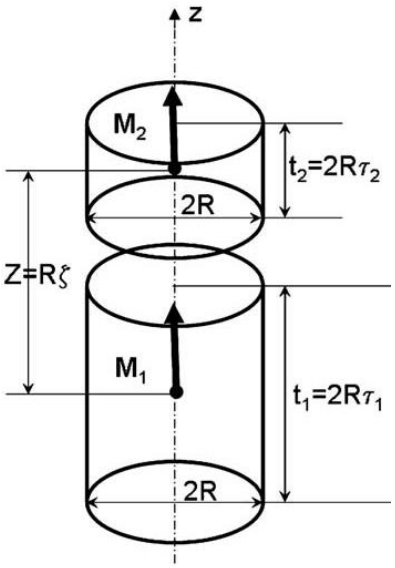

Figure 15. Magnet arrangement (Vokoun 2009)

By adapting this analytical expression into a suite of MATLAB scripts, we were able to compute the magnetostatic force between permanent magnets as a function of end-to-end separation distance, radius, thickness, and saturation magnetization, as well as solve the inverse problem of finding the separation distance required to yield a desired magnetostatic force. Our code matched the test cases in Vokoun et al. and also an independent simulation in the commercial multiphysics software COMSOL.

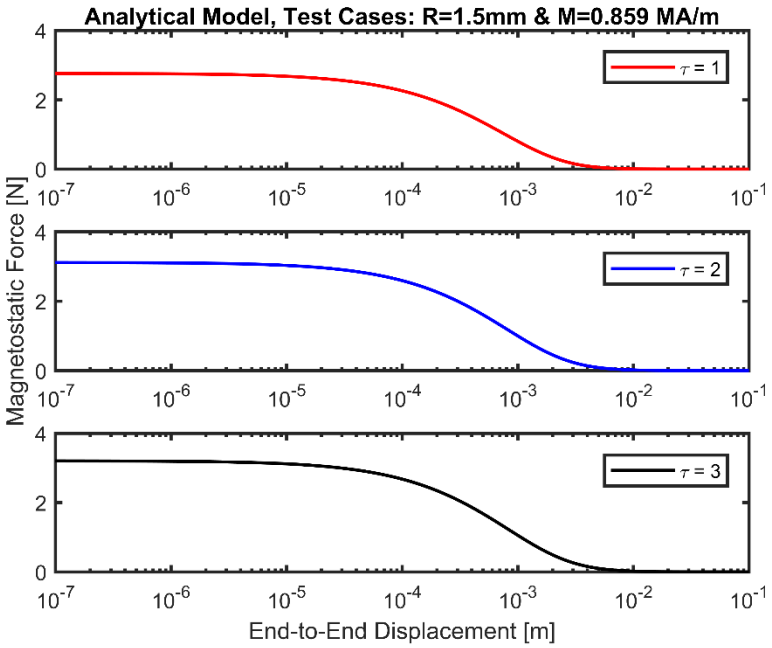

Figure 16. Attraction forces for varied aspect ratios

Since at large distances the magnetostatic force is asymptotic to x^{-4} on axis and x^{-8} off axis (Vokoun 2009), we ensured that the cylindrical permanent magnets were fastened with axes aligned coincidently in the vertical direction in all designs. We performed pull force experiments on real magnets to compare with the analytical model, as detailed next.

4.4. Magnet Experiments

Team A&E developed an experimental protocol to obtain contact forces and force displacement curves for a set of commercially purchased nickel-plated neodymium cylindrical permanent magnets. These rare earth magnets resist demagnetization from certain sources and are fairly corrosion resistant. The magnets ordered and tested were 1/2 inch diameter 24 lb pull, 1/2 inch diameter 19 lb pull, and 3/8 inch diameter 10 lb pull permanent magnets, where pull rates in some sense the strength of the magnet itself. The masses are, respectively, 12.1 grams, 11.9 grams, and 5.0 grams. Each type had a thickness (height) identical to its diameter.

We designed and additively manufactured a series of custom test fixtures that were mounted to a table. A digital force gauge measured the magnetostatic interaction force as the device pulled in a single direction one test magnet away from another magnet fixed in the AM test stand. The experiment began by recording the distance between the fixed magnet and test magnet, both of the same strength and radius. By using the hook on the force gauge to pull the test magnet away from the magnetic field of the other, the peak pull force (in Newtons) is recorded for three trials total at the same distance, then averaged the forces to yield a single data point for that distance. This process is repeated for increasing distances calibrated with 0.92 mm washers acting as discrete spacers. Data was recorded from 0 mm separation (corresponding to contact force) to 17.84 mm separation for both the 24 lb pull and 19 lb pull magnets and from 0 mm to 11.04 mm for the 10 lb pull magnets. After obtain the three sets of data for each type of magnet, the points were compared with the analytical magnetic force model.

This page is intentionally left blank.

5. RESULTS

5.1. Final Solutions

PASS

The final iteration of the PASS design is shown in figure 17. The red cylinder in the center is the additively manufactured *seismic mass* with final mass of 0.110 lbm. Imbedded in the seismic mass are ball bearings to reduce friction and complete the circuit; these ball bearings travel along channels within the chamber. The seismic mass is suspended from a 13 lbf/in linear spring, and contained within an AM body.

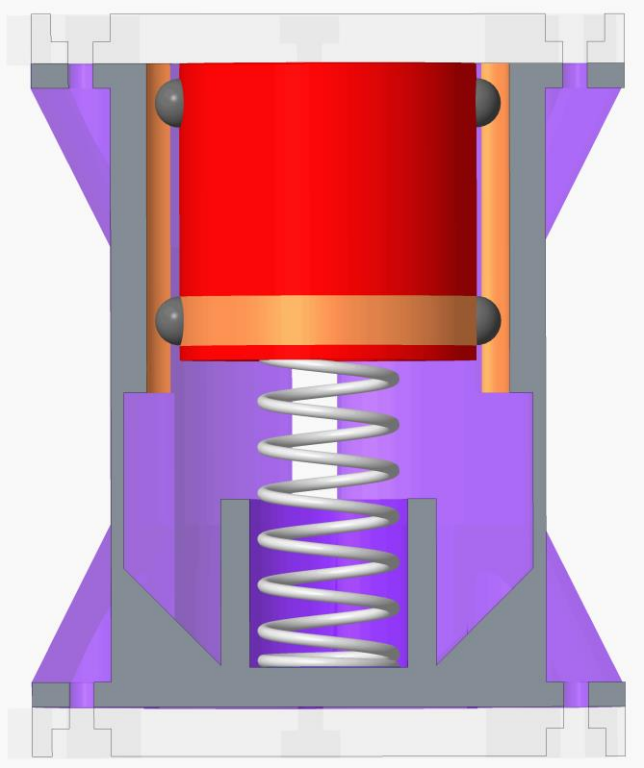

Figure 17. PASS final product

Circuit connections are completed by the two lower ball bearings horizontally attached in series with copper tape. These bearings initially start in contact with multiple adjacent strips of copper tape aligned vertically on the device, maximizing surface contact and decreasing resistance. Upon shock input, the seismic mass displaces with the ball bearings sliding along the electric channel until reaching a threshold of 0.4 inches; the lowest two ball bearing then fall into separate slots, removing electric contact with the horizontal trace of copper tape.

Printing of the PASS was done entirely on a MakerBot Replicator and the material used was PLA. This material was chosen primarily due to time constraints. The tolerances could be greatly improved through the use of more advanced printers and different materials. Furthermore, in

order to allow for experimental verification of the dynamic analysis, vertical slots were designed into the case and offset 90 degrees from the ball bearing channels.

MSF

The final iteration of the Magnet Shock Failsafe design is shown in figure 18. The red cylinders located in the middle of the mechanism are the *actuating magnets*. These are 24 lb pull neodymium permanent cylindrical magnets of identical radius and have been tuned to either separate or remain attached depending on the system input. They are physically separated by a 1 mm surface to prevent any ill effects from direct contact. The purple cylinder is a 3D printed spacer with tuned height placed between the actuating magnets to guarantee that the device triggers correctly upon the two input shocks.

The upper and lower extremities of the mechanism house the *catching magnets*. These are 28 lb pull neodymium permanent cylindrical magnets of equal radius. The function of the catching magnets is to irreversibly attract the actuating magnets as they displace upon escape. The distance between the actuating magnets and the catching magnets was designed to be sufficiently far enough such that the catching magnet fails to exert a noticeable force on the actuating magnet in the mechanisms untriggered state. In the top and bottom cavities, the inner surface is contoured to prevent a free falling magnet from reentering the middle chamber.

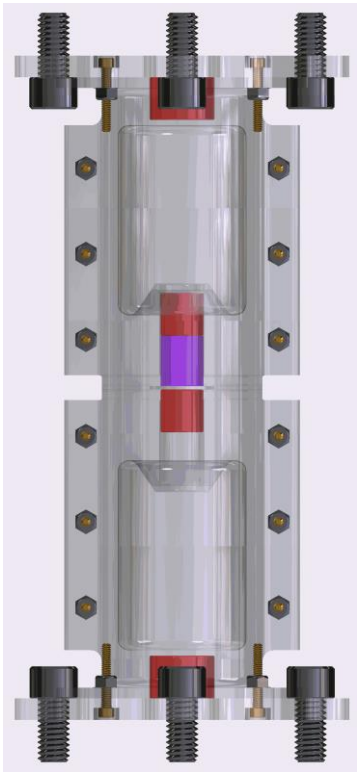

Figure 18. MSF final product

We ran copper tape through one side of the middle of the mechanism, making electrical contact with the lower nickel-plated actuating magnet. This magnet completes a circuit by making

conductive contact with additional tape placed on the other side. When the magnet separates due to specified shock input, the electrical channel is opened.

Further, the mechanism was printed on a Stratasys Objet30 3D printer. Specifically, VeroClear resin was used for a transparent finish, allowing for clear observation the interactions between the magnets during drop testing. Observing the magnet behavior during testing is crucial for an empirical understanding of the separation behavior of the magnet interaction. The manufacturer specifications were experimentally tested to ensure manufacturing defects were minimal. Finite element and multiphysics simulations, analytical models, experimental testing, and iterative adjustments compose the engineering approach we used to quantify the magnetostatic force, escape energy, and optimal magnet separation distance.

5.2. Analysis

PASS

Applying the maximax method to the PASS, we obtain the relative displacement SRS for the SDOF system. That is, given the natural frequency of the PASS, the peak absolute displacement of its seismic mass can be read off of the plot of the spectrum, and vice versa. In particular, the latter is especially useful in the design of the components in the PASS. We require a spring with a certain spring constant that will yield a predetermined mass displacement in order for the motion to trigger the ball bearing failsafe mechanism. Given the SRS, we simply read off the required natural frequency to displace the mass by this amount, and then iterate using the expression for natural frequency to match up a purchasable spring with a reasonable value of mass that can be feasibly additively manufactured.

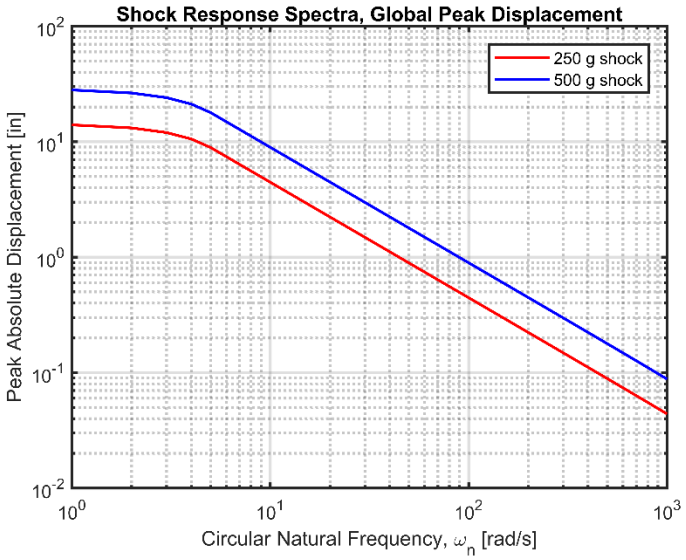

Figure 19. PASS displacement SRS

With this design tool in hand, we created the final version of PASS with a 0.05 kg (0.11 lb) mass. Mass was increased to this value from a lower mass AM component by fixing a modular stack of to the top of this structure. Team A&E purchased a helical spring with a 2276.7 N/m (13

lb/in) spring constant, yielding a natural frequency of the system $\omega_n = 213.4$ rad/s. Its dimensions are an 18.3 mm (0.72 inch) outer diameter and 43.2 mm (1.7 inch) length, with closed and flat ends.

For the PASS, we assumed a damping ratio of $\zeta = 0.05$ in accordance with industry standards. Reading off the value from the displacement SRS for PASS, we obtain a displacement of 0.42 inches for a 500 *g* haversine shock.

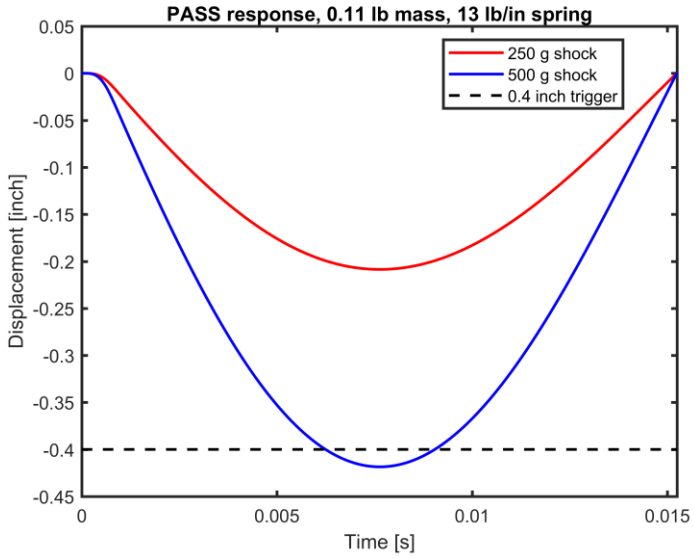

Figure 20. PASS activation threshold

The trigger threshold for the mechanism was set to 0.4 inch peak displacement of the seismic mass. Figure 20 shows the solution to the ODE equations of motion with both 250 and 500 *g* haversine shock inputs. We would clearly expect the mass to displace approximately 0.2 inches at 250 *g* loading and 0.4 inches at a 500 *g* loading.

MSF

The FEA Abaqus analysis of max principle stress contours of the magnetic shock failsafe output a global peak value of approximately 11 MPa near a corner of the MSF, where the stress is highly concentrated. However, since PLA fails on the order of 100 MPa, we conclude that the MSF will not fail due to fracture from a 500 *g* input haversine shock.

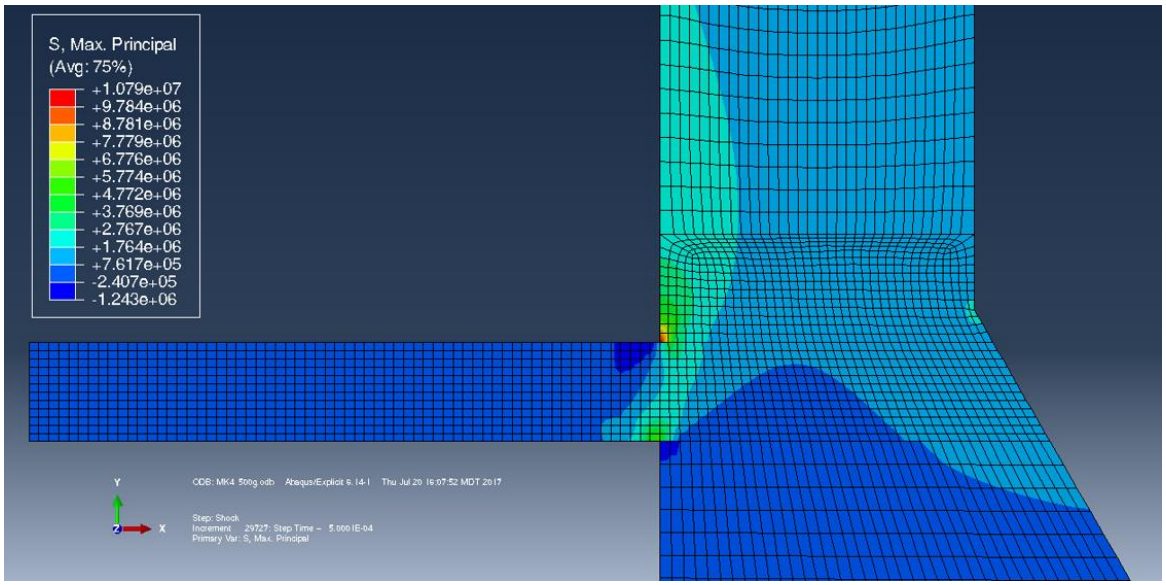

Figure 21. Fracture simulation

Using the same 2D model in Abaqus, a modal analysis was run on the structure. The frequency corresponding to the greatest response of the structure when a shock is imparted into the system is $1/T$ Hz, or 1000 Hz for the 1 ms haversine. However, the first mode has a natural frequency of 3336 Hz, which is well above this peak response frequency. If we assume the MSF is a SDOF system, then at higher mode frequencies the response of the structure approaches the peak acceleration loading of the shock. In effect, the structure is stiffer at higher and higher natural frequencies and its response will be more predictable than if the natural frequencies were below 1000 Hz. One advantage of natural frequencies in the low frequency regime is that the structure will be more isolated to vibration (Palm 2013), and the response of the part will be less than the peak shock loading. However, the final MSF clearly avoids any damaging resonant effects because of its high first natural frequency.

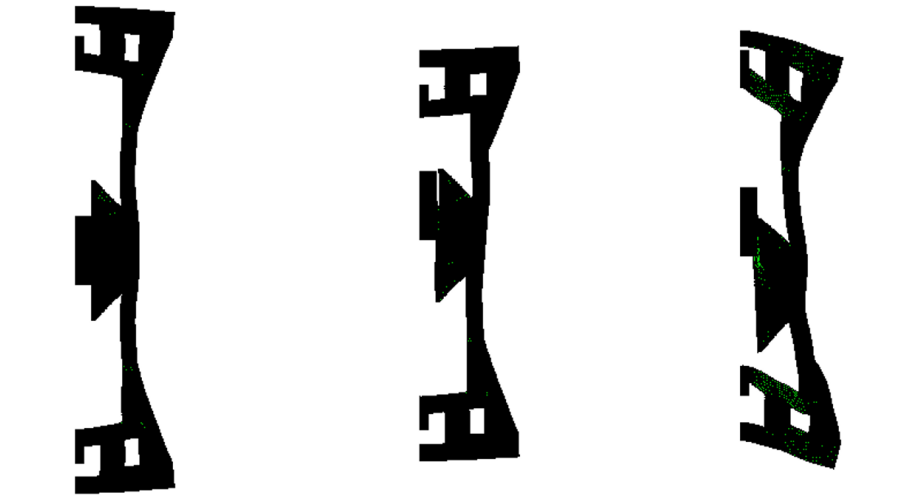

Figure 22. Mode shapes and natural frequencies

After obtaining experimental magnetostatic force data from the pull force testing experiments, we computed an approximation to the magnet's saturation magnetization to best fit the data to the analytical model. The saturation magnetization is a material dependent property of the magnet. The contact force measurement was far off from the analytical curve fit, likely due to the inability to physically make perfect contact with the two magnetic surfaces; thus, we exclude the contact force point at 0 mm. Using nonlinear optimization by minimizing the mean square error, we obtain the following optimal magnetization values:

Table 1. Saturation magnetization results

Magnet [lb pull]	Saturation Magnetization *M* [MA/m]
24	1.063
19	0.905
10	0.875

Using these calculated saturation magnetizations, we can overlay the plots of the experimental force data onto the analytical model. We observe an extremely close match and have high confidence that our magnets agree with the model.

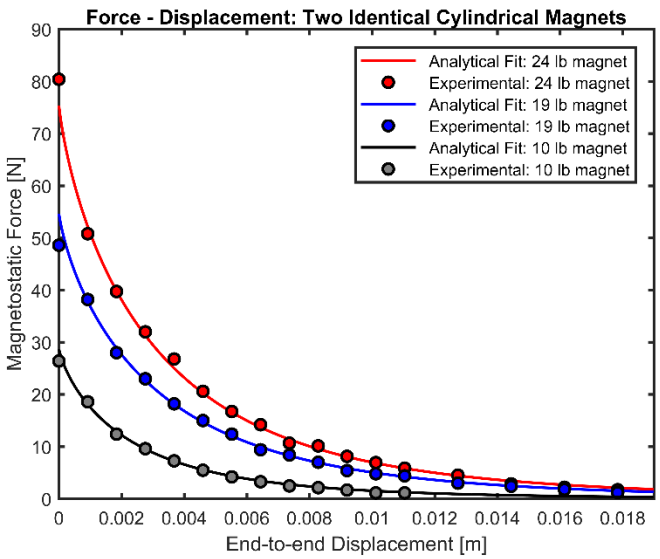

Figure 23. Experimental data fit

With the validated analytical model in hand, we now proceed to compute the separation distance required for the actuating magnet to completely separate and stick to the catching magnet at the bottom. An energy approach is used, akin to the concept of an "escape velocity". We need to compute the work required to displace the actuating magnet from some initial separation to an infinite separation distance away from the fixed magnet and its magnetic field. This work-energy principle applied to the design of the MSF is given as

$$\begin{aligned}\int_{x_c}^{\infty} F_z(x)\,dx &= (KE)_{shock} + (PE)_{gravity} \\ &= \frac{1}{2}m(\Delta V)^2 + mg(\Delta h) \\ &= \frac{1}{8}mA^2T^2 + mg(\Delta h)\end{aligned}$$

where $F_z(x)$ is the magnetostatic force, m is the mass of the actuating magnet, x_c is the required separation distance for the actuating magnet to escape, and Δh is the distance from the bottom surface of the actuating magnet in its initial attached position to the internal bottom cavity surface of the MSF. Given physical constraints and numerical accuracy errors, it is unnecessary to compute the work required to move the actuating magnet infinite distance away from its original position; thus, we settle on an approximation of this improper integral using

$$\int_{x_c}^{1\text{ meter}} F_z(x)\,dx = \frac{1}{8}mA^2T^2 + mg(\Delta h)$$

where the right hand side is constant and x_c is the target variable to be determined. For the MSF, $\Delta h = 64.8$ mm, so a 1 meter target for the upper limit of the work integral is more than sufficient for our purposes. We solve for x_c in MATLAB and obtain the following table for a 10% buffer on our peak input shock bounds:

Table 2. Escape energy model results

Magnetic Separation Distance, 10% buffer			
Magnet [lb pull]	Minimum [mm], 450 g	Chosen [mm], $500 \cdot \cos 45° \, g$	Maximum [mm], 275 g
24	11.71	**14.9**	18.14
19	9.25	**12.15**	15.06
10	6.32	**8.45**	10.59

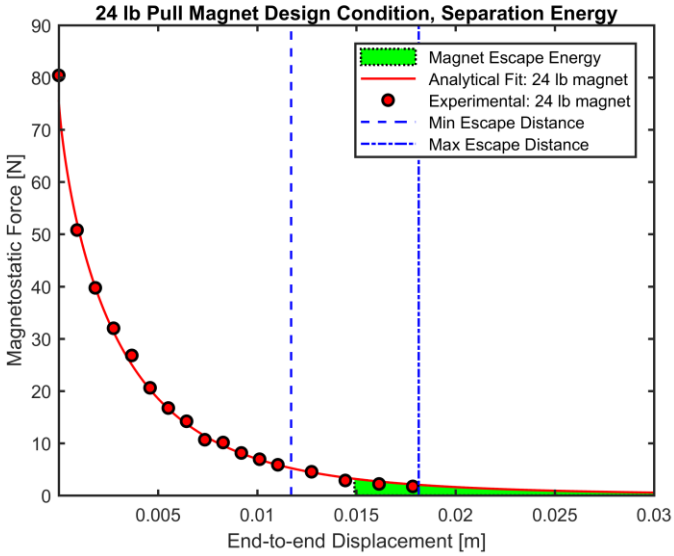

Figure 24. MSF design conditions

We tested the MSF on the drop table with the 24 lb pull magnets separated by 14.9 mm above the built-in 1 mm spacing.

5.3. Shock Testing

PASS

From the high speed footage of the PASS, it is clear that the system acted as designed. Each line marked on the PASS represents 0.1 inch displacement, and the top, longest, line representing the initial position. During the experiment, the seismic mass displaced approximately 0.4 inches and successfully triggered.

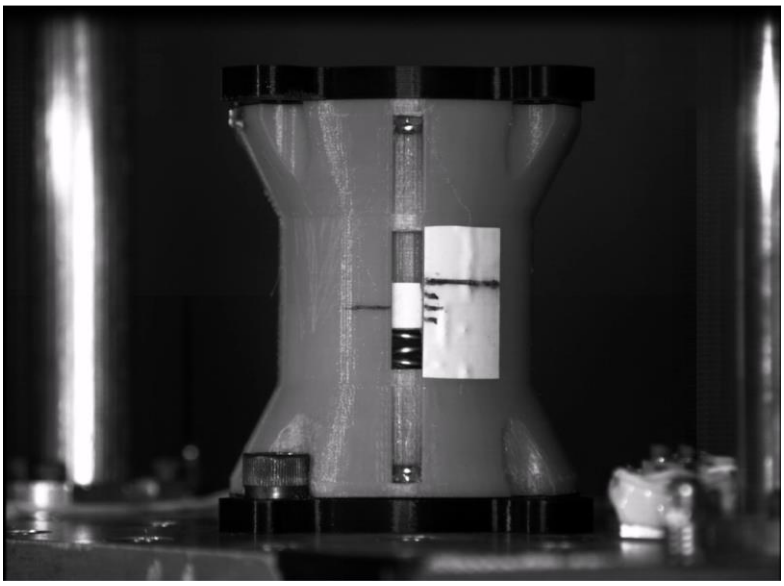

Figure 25. PASS 500 *g* High Speed Footage

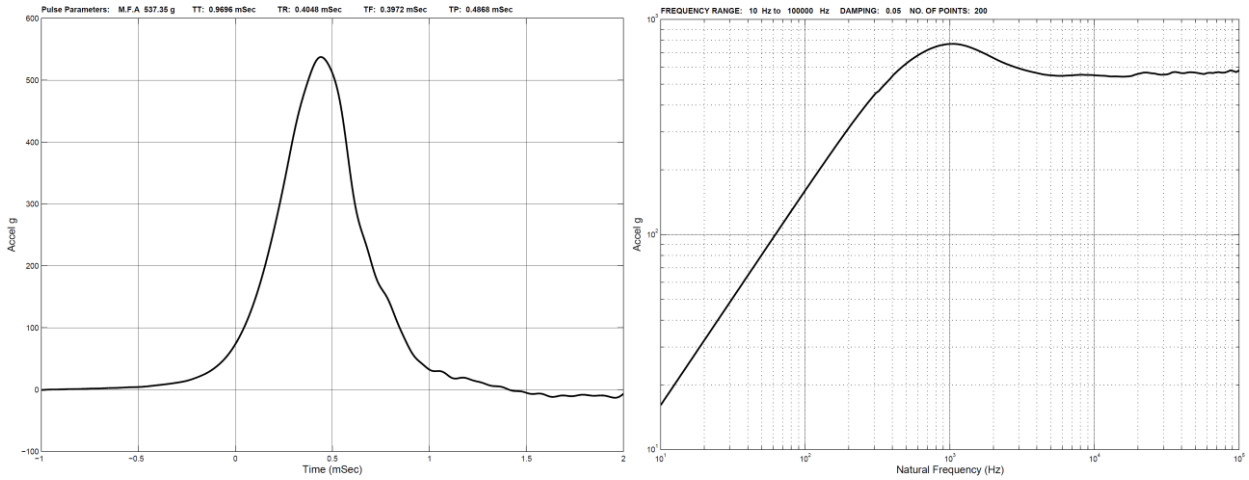

Figure 26. PASS input 500 *g* shock profile (left), SRS (right)

Table 3. PASS shock table testing results

PASS Mark II: 0.11 lb mass, 13 lb/in spring			
Peak Loading [g]	Resistance before [Ω]	Resistance after [Ω]	Trigger state
250	7.8	7.8	No
500	8.8	∞	Yes

MSF

Viewing figure 27, from left to right, top to bottom, the footage confirms that the device successfully triggered in the expected manner. The lower actuating magnet begins to separate from the centerline upon a 500 *g* shock input. Once separated, the magnet continues traveling downwards until being pulled into the lower most catching magnet.

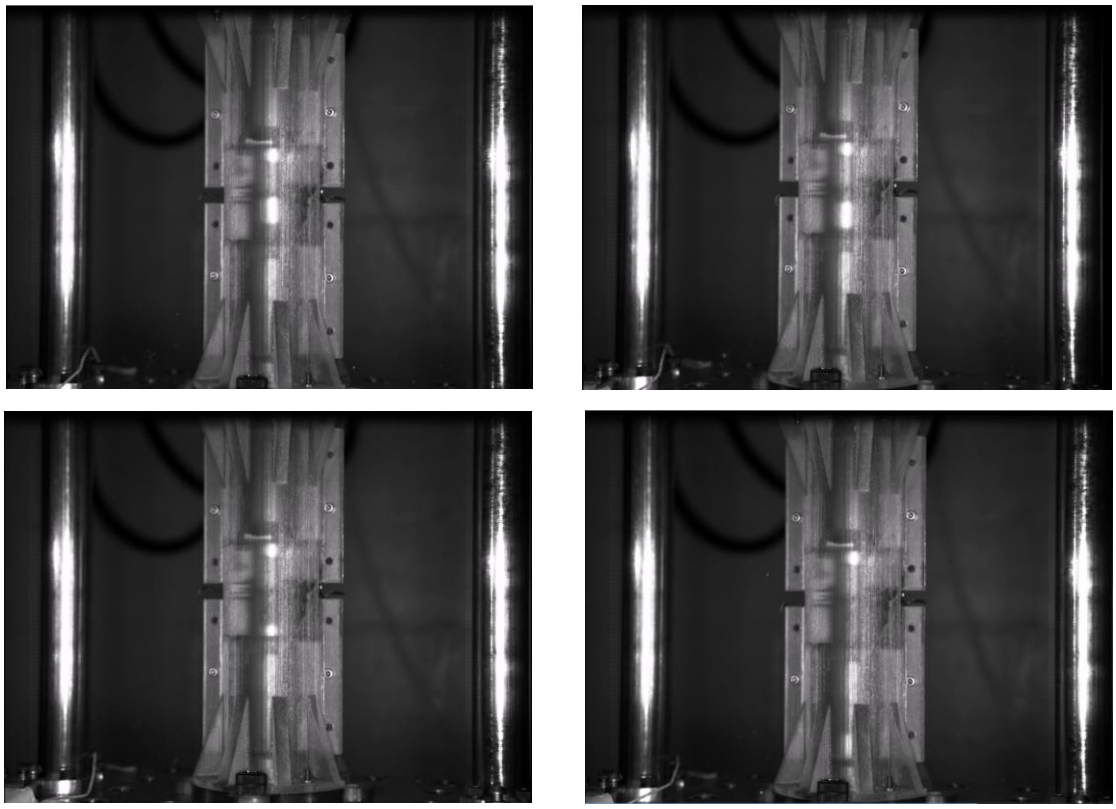

Figure 27. MSF 500 *g* High Speed Footage

Table 4. MSF shock table testing results

MSF Mark II, 24 lb pull magnets			
Peak Loading [*g*]	Resistance before [Ω]	Resistance after [Ω]	Trigger state
250	0.8	0.8	No
500	0.7	∞	Yes

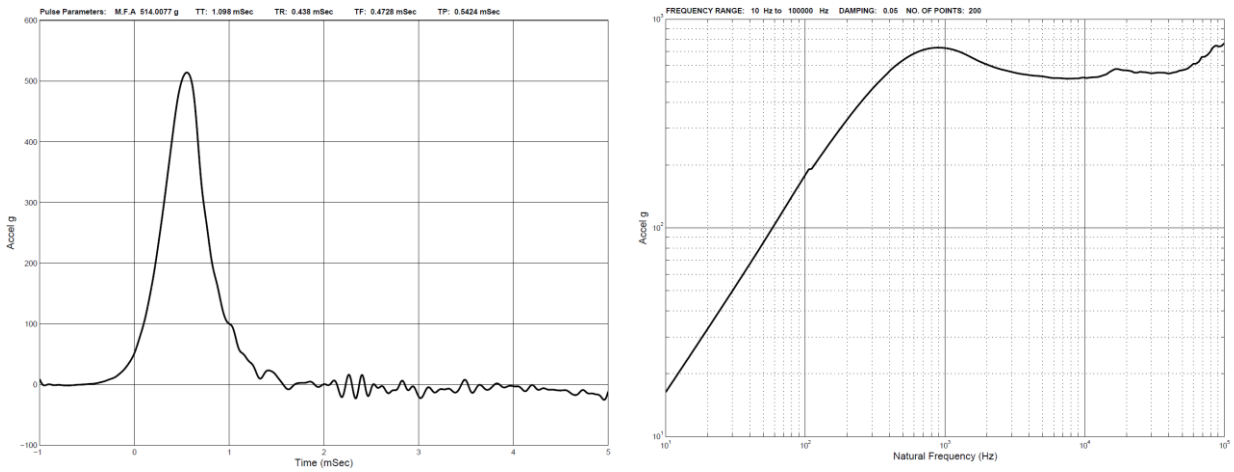

Figure 28. MSF input 500 *g* shock profile (left), SRS (right)

This page is intentionally left blank.

6. DISCUSSION

Team A&E successfully met all NW SPRINT requirements with two highly iterated yet innovative final solutions. We have outlined a set of concepts for potential passive shock failsafes, and have demonstrated the feasibility of two such mechanisms: the passive accelerometer spring system and the magnetic shock failsafe. These devices are primarily additively manufactured, and the parts purchased from outside vendors were tested in-house to verify specifications and quality. Detailed theoretical and computational analyses were performed to validate and design the failsafe devices. Moreover, the PASS benefits from vibration isolation since its natural frequency of 34 Hz is significantly lower than 1000 Hz. Both the PASS and MSF were tested on the Sandia drop tables, where high speed video capture and digital multimeter measurements of resistance confirmed actuation of the two mechanisms in 500 *g* input shock environments. A summary of product qualification is given below.

Table 3. Objectives met

Requirements	PASS 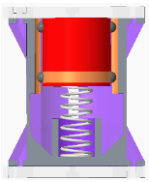	MSF 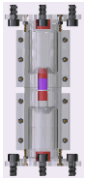
Percent AM (by volume)	98.70%	97.70%
8x8x8 inch envelope	YES	YES
One Electrical Channel	YES	YES
Remain untriggered at 250 g	YES	YES
Irreversibly trigger at 500 g	YES	YES
< 10 ohm resistance untriggered	YES (8.8 ohm)	YES (0.8 ohm)
> 10 megaohm resistance triggered	YES	YES
Senses shock in at least one direction	YES	YES

The PASS mechanism has clearly been designed to scale based on size. The parameters able to vary are the mass, spring constant, and peak response displacement. Given any two of the former, the third can be computed immediately. Therefore, the mechanism can be optimized for a small mass and spring for uses in MEMs devices, for example. Scaling in the manufacturing perspective should be considered as well. The mechanism is fairly simple in design with few parts to assemble; large volume production is surely possible. Irreversibility emerges from the ejection of ball bearings during the triggering sequence. Once the electrical contacts (ball bearings) have been removed, the circuit cannot close again.

The MSF is highly versatile. Any pair of magnets can be tuned with respect to a specific separation distance to perform optimally. Physical drop tests have validated this claim, in which the MSF functioned as designed in shock environments. The size of the mechanism can be reduced depending on the magnets themselves, so the MSF can be miniaturized for use in environments constrained by total space available. The irreversibility of the MSF stems from the catching magnets placed at the extremities of the mechanism. By decreasing the distance between both actuating magnets in the untriggered state, the shock amplitude required to expel one magnet can be order of magnitudes higher than those considered in this work. For example, in the current design, a shock greater than 1200 g is required to separate one actuating magnet given the smallest possible 1 mm separation distance. In future design iterations of the MSF, the actuating and catching magnets can be reduced in size depending on the shock input.

Limitations

We acknowledge some limitations of the PASS mechanism in this work. Due the metallic nature of the spring, there is some possibility of creep or strain deformation occurring at some point over the component's long term lifespan. Wear and corrosion of the sliding ball bearings must be also be taken into account. With respect to the functionality of the design, there is a possibility that the ball bearings do not fully deploy, becoming jammed in the channel. Lastly, copper tape could come into contact with the copper tape placed in the bearing channel as a result of dislocation during impact. This problem can be solved by inserting conductive traces through the seismic mass.

Magnet deterioration is a limitation of the MSF. Based on project experience, the nickel plated coating can be easily removed through consistent, high energy impact. This can pose a problem to electrical circuitry within the mechanism throughout the lifetime of the component. Additionally, magnets may deteriorate in field strength over the course of decades. Electrical components might be affected by changing magnetic fields, so we would require a way to encase the susceptible component in magnetic shielding material.

Future Work

There exists much potential for future directions and improvements of this research. Additional MSF shock testing at boundary distances would verify the analytical separation distance range computed with the work-energy principle and allow for any adjustments to the mathematical models as necessary. Improved numerical techniques are needed to reduce numerical errors in improper integral computations for escape energy calculations.

Furthermore, housing designs must be explored to incorporate shock sensing in three axial directions. First steps have been taken in this regard; the MSF is designed to trigger at shock loads input at 45 degrees to the normal, representing the minimum acceleration component that could be imparted to the system in two dimensions. Early solutions for six degrees of freedom passive shock sensing include a three-dimensional array of MSFs that are electrically coupled together.

Due to time constraints, additively manufactured conductive inserts could not be used in the final MSF product. However, using AM conductive inserts to replace the currently used copper tape would be a major improvement. Lastly, multi-material AM capabilities would allow for interlocked printing of both conductive material for traces and standard material for future iterations of the MSF.

Both the PASS and MSF are highly scalable mechanisms in terms of size and weight. Our analytical techniques allow us to tune these systems to respond favorably to any arbitrary input waveform with finite kinetic energy. By being irreversible when switched into the triggered state and high resettable, these concepts can be further developed into failsafe components in larger systems used for a variety of critical applications.

This page is intentionally left blank.

REFERENCES

1. Broch, J. T. (1980). *Mechanical vibration and shock measurements*. Brüel & Kjær.
2. Camescasse, B., Fernandes, A., & Pouget, J. (2014). Bistable buckled beam and force actuation: Experimental validations. *International Journal of Solids and Structures*, *51*(9), 1750-1757.
3. Cazottes, P., Fernandes, A., Pouget, J., & Hafez, M. (2009). Bistable buckled beam: modeling of actuating force and experimental validations. *Journal of Mechanical Design*, *131*(10), 101001.
4. Frangi, A., De Masi, B., Confalonieri, F., & Zerbini, S. (2015). Threshold Shock Sensor Based on a Bistable Mechanism: Design, Modeling, and Measurements. *Journal of Microelectromechanical Systems*, *24*(6), 2019-2026.
5. Gaberson, H. A. (2007). Pseudo velocity shock spectrum rules for analysis of mechanical shock. *IMAC XXV, Orlando, FL*.
6. Good, R. H. (2001). Elliptic integrals, the forgotten functions. *European Journal of Physics*, *22*(2), 119.
7. Irvine, T. (2002). An introduction to the shock response spectrum. *Rev P, Vibrationdata*.
8. Lalanne, C. (2009). Mechanical Vibration and Shock: Mechanical Shock (Volume 2).
9. Lang, G. F. (2003). Shock'n on Shakers. *Sound and Vibration*, *37*(9), 12-21.
10. Palm III, W. (2013). *System dynamics*. McGraw-Hill Higher Education.
11. Qiu, J., Lang, J. H., & Slocum, A. H. (2004). A curved-beam bistable mechanism. *Journal of microelectromechanical systems*, *13*(2), 137-146.
12. Smallwood, D. O. (1981). An improved recursive formula for calculating shock response spectra. *Shock and Vibration Bulletin*, *51*(2), 211-217.
13. Smallwood, D. O. (1986). Shock response spectrum at low frequencies. *The Shock and Vibration Bulletin, SAVIAC*, *1*, 279-288.
14. Smallwood, D. O. (1994). Characterization and simulation of transient vibrations using band limited temporal moments. *Shock and Vibration*, *1*(6), 507-527.
15. Vijaya, M. S. (2012). *Piezoelectric materials and devices: applications in engineering and medical sciences*. CRC Press.
16. Vokoun, D., Beleggia, M., Heller, L., & Šittner, P. (2009). Magnetostatic interactions and forces between cylindrical permanent magnets. *Journal of magnetism and Magnetic Materials*, *321*(22), 3758-3763.
17. Walter, P. L. (2005) The Shock Spectrum: What Is It?. *Technical Note TN-19, http://www. pcb. com/techsupport/docs/vib/, PCB Piezotronics, Inc*.
18. Zhang, Y., Liu, Y., & Wang, Z. L. (2011). Fundamental theory of piezotronics. *Advanced Materials*, *23*(27), 3004-3013.

This page is intentionally left blank.

DISTRIBUTION

MS0333	Audrey Morris-Eckart	Org. 2616
MS0344	Lindsay Klennert	Org. 2624
MS0374	M. Fran Current	Org. 2276
MS0428	Tom Woodall	Org. 9430
MS0899	Technical Library	9536 (electronic copy)

This page is intentionally left blank.


Sandia National Laboratories